

Photoelectron Imaging and Spectroscopy of MI_2^- ($M = Cs, Cu, Au$): Evolution from Ionic to Covalent Bonding[†]

Yi-Lei Wang,[‡] Xue-Bin Wang,^{§,||} Xiao-Peng Xing,^{§,||} Fan Wei,[‡] Jun Li,^{*,‡} and Lai-Sheng Wang^{*,⊥}

Department of Chemistry & Key Laboratory of Organic Optoelectronics and Molecular Engineering of Ministry of Education, Tsinghua University, Beijing 100084, China, Department of Physics, Washington State University, 2710 University Drive, Richland, Washington 99354, Chemical & Materials Sciences Division, Pacific Northwest National Laboratory, MS K8-88, P.O. Box 999, Richland, Washington 99352, and Department of Chemistry, Brown University, Providence, Rhode Island 02912

Received: April 8, 2010; Revised Manuscript Received: April 28, 2010

We report a combined experimental and theoretical investigation of MI_2^- ($M = Cs, Cu, Ag, Au$) to explore the chemical bonding in the group IA and IB diiodide complexes. Both photoelectron imaging and low-temperature photoelectron spectroscopy are applied to MI_2^- ($M = Cs, Cu, Au$), yielding vibrationally resolved spectra for CuI_2^- and AuI_2^- and accurate electron affinities, 4.52 ± 0.02 , 4.256 ± 0.010 , and 4.226 ± 0.010 eV for CsI_2 , CuI_2 , and AuI_2 , respectively. Spin–orbit coupling is found to be important in all the diiodide complexes and ab initio calculations including spin–orbit effects allow quantitative assignments of the observed photoelectron spectra. A variety of chemical bonding analyses (charge population, bond order, and electron localization functions) have been carried out, revealing a gradual transition from the expected ionic behavior in CsI_2^- to relatively strong covalent bonding in AuI_2^- . Both relativistic effects and electron correlation are shown to enhance the covalency in the gold diiodide complex.

I. Introduction

The chemical bond is the most important concept in modern chemistry. Traditionally chemical bonds are classified as covalent or ionic in molecular systems. The group IB halides are usually considered as ionic compounds. However, because of the strong relativistic effects,¹ gold has been found to display chemistry very different from its lighter congeners.^{2,3} Specifically, significant covalent bonding character has been increasingly found in gold-containing compounds,⁴ from the well-known $Au(CN)_2^-$ complex^{5–7} to the simple gold oxide and sulfide molecules.⁸ A question arises if the gold halide molecules may in fact contain covalent characters. Because iodine possesses the lowest electron affinity among the halide elements and it is very close to that of gold, we suspect that significant covalent bonding may exist between Au and I. Therefore, in the current article we investigate the evolution of chemical bonding in the coinage iodide complexes, MI_2^- ($M = Cu, Ag, Au$) using the more ionic CsI_2^- complex as a reference.

Gold halides form interesting solid materials,⁹ and the electronic structures of gaseous gold halide molecules have been investigated in a number of previous computational studies,^{10–12} in particular, regarding the relativistic effects in these molecules.^{13–16} The gold dihalide complexes AuX_2^- ($X = Cl, Br, I$) have been investigated previously using photoelectron spectroscopy (PES) and mass spectrometry,¹⁷ with an emphasis on the production of divalent gold(II) species, AuX_2 , upon electron detachment from the AuX_2^- anions. The PES data on AuX_2^- have stimulated a

number of theoretical studies for detailed spectral assignments.^{18–20} The importance of spin–orbit (SO) coupling for the assignment of the PES spectra has been pointed out by Misha et al.,¹⁹ whose calculations including SO effects yielded quantitative agreement with the experimental data reported in ref 17.

In the current study, we present a joint experimental and theoretical investigation on the coinage metal diiodide complexes, MI_2^- ($M = Cu, Ag, Au$), emphasizing on the evolution of chemical bonding from Cu to Au. The ionic CsI_2^- complex is included as a reference. Both photoelectron imaging and low-temperature PES data have been obtained for MI_2^- ($M = Cs, Cu, Au$). The AgI_2^- complex could not be studied experimentally using the electrospray source due to the low solubility of AgI . Vibrationally resolved PES spectra have been obtained for CuI_2^- and AuI_2^- at 266 nm, as well as rich electronic structure information at 193 nm using vibrationally cold anions. Density functional theory (DFT) and ab initio calculations are carried out on the four MI_2^- species to help spectral interpretation and chemical bonding analyses. As expected, SO coupling effects are found to be important for all the diiodide complexes. Our theoretical analyses reveal typical ionic bonding behavior in CsI_2^- and significant covalent character in AuI_2^- , while that in CuI_2^- and AgI_2^- is found to be between the ionic and covalent bonding.

II. Experimental Methods

The MI_2^- ($M = Cu, Au, Cs$) complexes were produced using electrospray ionization (ESI), and the photodetachment experiments were performed using two methods: photoelectron imaging²¹ and low-temperature PES with a magnetic-bottle photoelectron analyzer.²² The AgI_2^- complex was omitted in the experiment due to the low solubility of AgI .

A. Photoelectron Imaging. The photoelectron imaging experiment was carried out on a room temperature ESI-PES

[†] Part of the “Klaus Müller-Dethlefs Festschrift”.

* To whom correspondence should be addressed, junli@tsinghua.edu.cn and Lai-Sheng_Wang@brown.edu.

[‡] Tsinghua University.

[§] Washington State University.

^{||} Pacific Northwest National Laboratory.

[⊥] Brown University.

apparatus²³ by replacing the original magnetic-bottle photoelectron analyzer with a velocity-map imaging system, details of which have been described elsewhere.²¹ About 1 mM solutions of CsI and AuI in water/methanol mixed solvents (1/3 volume ratio) or CuI in pure acetonitrile were used as electrospray solutions to generate the respective MI_2^- complexes. Anions from the ESI source were directed into an ion trap via a rf-only ion guide. After a trapping time of 0.1 s, the ions were pulsed out into a time-of-flight mass spectrometer and directed into the center of the photoelectron imaging system, where they were detached by a linearly polarized laser beam at 266 nm. The nascent electron cloud was accelerated by a high voltage pulse applied to the imaging electrodes and was projected onto a phosphor screen behind a set of microchannel plates. The positions of the photoelectrons on the phosphor screen were recorded by a CCD camera and accumulated as a photoelectron image. The usual accumulation time was about 10^5 laser shots at a 10 Hz repetition rate. Since the laser polarization was parallel to the surface of the microchannel plates and the phosphor screen detector, the original shape of the three-dimensional electron clouds could be rebuilt through inverse Abel transformation from the recorded two-dimensional images, which were performed using the BASEX program.²⁴ The electron binding energy spectra and photoelectron angular distributions were obtained from the rebuilt three-dimensional images. The electron kinetic energy resolution of our imaging system is about 2.5% for 1 eV electrons, as calibrated from the 266 and 355 nm spectra of Br^- and I^- .²¹

B. Low-Temperature Photoelectron Spectroscopy. The low-temperature PES experiment was carried out using a magnetic-bottle apparatus coupled to an ESI source and a cryogenically controlled ion trap.²² Anions from the ESI source were guided by a series of rf-only quadrupole devices into a Paul trap, which is connected to the coldfinger of a closed cycle He refrigerator (10–350 K). The ions were accumulated and cooled in the ion trap before being pulsed into the extraction zone of a time-of-flight mass spectrometer. The MI_2^- species were mass-selected and decelerated before being detached by 193 nm photons (6.424 eV) from an ArF excimer laser or 266 nm photons (4.661 eV) from a Nd:YAG laser in the interaction zone of a magnetic-bottle photoelectron analyzer operated at a 20 Hz repetition rate with the ion beam on and off on alternating laser shots for background subtraction. Photoelectrons were collected at near 100% efficiency by the magnetic bottle and analyzed in a 5.2 m long electron flight tube. Time-of-flight photoelectron spectra were collected and converted to kinetic energy spectra calibrated with the known spectra of I^- and ClO_2^- . The electron binding energy spectra reported were obtained by subtracting the kinetic energy spectra from the respective detachment photon energies. The kinetic energy resolution ($\Delta E/E$) of the magnetic-bottle electron analyzer was 2% (i.e., 20 meV for 1 eV electrons).

III. Computational Methods

The theoretical investigations were performed using both DFT and wave function-based ab initio methods. The DFT calculations were performed using the generalized gradient approximation (GGA) with the PBE exchange-correlation functional²⁵ implemented in the Amsterdam Density Functional (ADF 2009.01) program.²⁶ The uncontracted Slater basis sets with the quality of triple- ζ plus two polarization functions (TZ2P) were used, with the frozen core approximation applied to $[1s^2-4d^{10}]$ for Cs and I, $[1s^2-3p^6]$ for Cu, $[1s^2-4p^6]$ for Ag, and $[1s^2-4f^{14}]$ for Au, respectively.²⁷ The AgI_2^- complex was also calculated

for completeness, even though no experimental data were presented. The scalar relativistic (SR) and SO coupling effects were taken into account by the zero-order-regular approximation (ZORA).²⁸ Geometries were optimized at the SR-ZORA level and single-point energy calculations were performed with inclusion of the SO effects. Vibrational frequency calculations were carried out to verify that the species were minima on the potential energy surface. The B3LYP hybrid functional was also used to optimize the MI_2^- anions with the Gaussian 03 program.²⁹ The basis sets used are the same as in the ab initio MOLPRO calculations described below.

To compare with the experimental PES spectra, we performed high-level ab initio calculations for MI_2^- ($M = Cs, Cu, Ag, Au$) using the MOLPRO 2008 program.³⁰ In these calculations we used both the CCSD(T) (coupled-cluster with single and double and perturbative triple excitations)³¹ and CASSCF (complete-active-space self-consistent field) methods.³² The geometries of MI_2^- were optimized with CCSD(T); single-point energies of the ground and excited states of the neutrals were calculated at the geometry of the anions at the same level. The electron binding energies corresponding to one-electron transitions from the closed-shell ground states of the MI_2^- anions to the ground and excited states of the MI_2 neutrals were obtained using a CASSCF/CCSD(T)/SO approach that was used previously for $M(CN)_2^-$ ($M = Cu, Ag, Au$).⁷ In this approach the SO splittings were treated as a perturbation to the scalar-relativistic state energies and were calculated on the basis of CASSCF wave functions with the diagonal matrix elements replaced by the CCSD(T) energies. The SO coupling effect was included by using a state-interacting method³³ with SO pseudopotentials. The valence orbitals, the 6s orbital for Cs, 3d and 4s for Cu, 4d and 5s for Ag, 5d and 6s for Au, and 5p for I, were included in the active space during the CASSCF calculations. As a result, we correlated 11 valence electrons in 7 active orbitals, denoted as CASSCF(11,7) for CsI_2 and CASSCF(21,12) for MI_2 ($M = Cu, Ag, Au$). The basis sets used were $(12s11p5d3f2g)/[8s8p5d3f2g]$ for Cs,³⁴ cc-pVTZ-PP for Cu, Ag, and Au,³⁵ and aug-cc-pVTZ-PP for I,³⁶ respectively. The effective core potentials with 46, 10, 28, 60, and 28 core electrons were used for Cs, Cu, Ag, Au, and I, respectively.^{34,36,37} For CuI_2^- , we noted larger than usual deviations (~ 0.2 eV) of the calculated VDEs related to detaching electrons from the Cu 3d δ_g orbital. Considering the necessity of balancing the $3d^{10-x}4s^{1+x}$ configurations involving the highly contracted Cu 3d orbitals,³⁸ a larger basis set with diffuse functions, aug-cc-pVTZ-PP,^{35,37} was used for Cu in the CCSD(T) single-point energy calculations, which led to excellent results.

IV. Experimental Results

Figure 1 shows the photoelectron images of MI_2^- ($M = Cu, Au, Cs$) recorded at 266 nm and room temperature. The photoelectron images for CuI_2^- and AuI_2^- are similar, both displaying one spectral band with similar electron kinetic energies and angular distributions. The image of CsI_2^- is very different, displaying much lower electron kinetic energies with isotropic angular distributions. The different angular distributions between the photoelectron images of the coinage diiodides and CsI_2^- suggest that they possess different electronic structures and different highest occupied molecular orbitals (HOMOs) from which an electron is detached. The electron binding energy spectra obtained from the images display vibrational fine features with a rather broad Franck–Condon envelope for CuI_2^- and AuI_2^- . The electron binding energies of CsI_2^- are much higher.

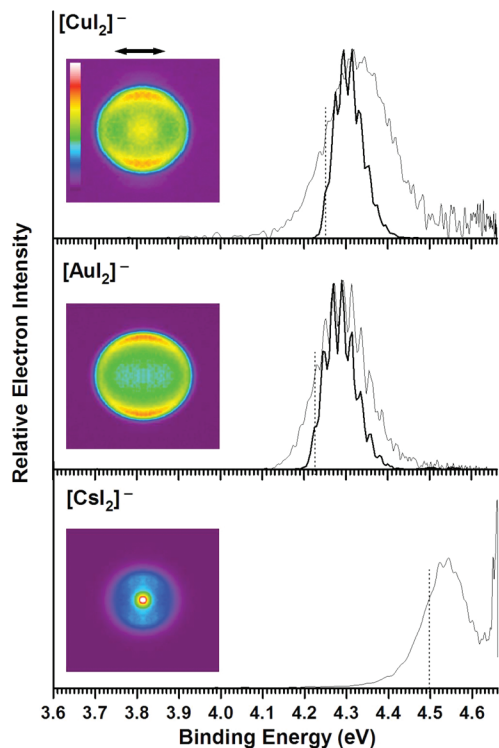


Figure 1. Photoelectron images of MI_2^- ($M = \text{Cs, Cu, Au}$) at 266 nm (inset), photoelectron spectra obtained from the images (gray curves), and 266 nm photoelectron spectra at 12 K (black curves). The double arrow represents the laser polarization. The vertical dot lines indicate the 0–0 transitions resolved in the 12 K spectra for CuI_2^- and AuI_2^- and adiabatic detachment energy estimated from the 266 nm spectrum of CsI_2^- at 12 K (not shown).

TABLE 1: Experimental Adiabatic Detachment Energies (ADEs) for MI_2^- ($M = \text{Cs, Cu, Au}$) and the Observed Totally Symmetric Vibrational Frequencies for the Ground State of CuI_2 and AuI_2

	ADE (eV) ^a	Vib. Freq. (cm ⁻¹)
CsI_2^-	4.52 ± 0.02	
CuI_2^-	4.256 ± 0.010	160 ± 15
AuI_2^-	4.226 ± 0.010^b	180 ± 15

^a Also represent the electron affinities for the corresponding neutral MI_2 species. ^b A less accurate value of 4.18 ± 0.07 was reported previously (ref 17).

In addition to the broad ground state band, the onset of a second band is observed in the 266 nm spectrum of CsI_2^- .

We have also obtained the PES spectra at 12 K for MI_2^- ($M = \text{Cu, Au, Cs}$) using the low-temperature magnetic-bottle apparatus.²² The 266 nm spectra at 12 K for CuI_2^- and AuI_2^- are superimposed on the spectra obtained with the imaging method at room temperature in Figure 1 (black thick curves). Because of the spectral cutoff associated with the magnetic-bottle apparatus, only a rising tail with an onset around 4.5 eV was obtained for CsI_2^- at 266 nm at 12 K (not shown). The effects of vibrational cooling at 12 K were dramatic. Due to the elimination of vibrational hot bands, the 12 K spectra were significantly sharpened. In particular, a single vibration progression was clearly revealed for CuI_2^- and AuI_2^- with frequencies of 160 ± 15 and 180 ± 15 cm⁻¹, respectively (Table 1). Because of the elimination of vibrational hot bands, the adiabatic detachment energy (ADE) for the ground state transition or the electron affinity of the corresponding neutral can be determined accurately, as marked by the dashed line in Figure 1. The obtained values are 4.256 ± 0.010 and 4.226 ± 0.010 eV for

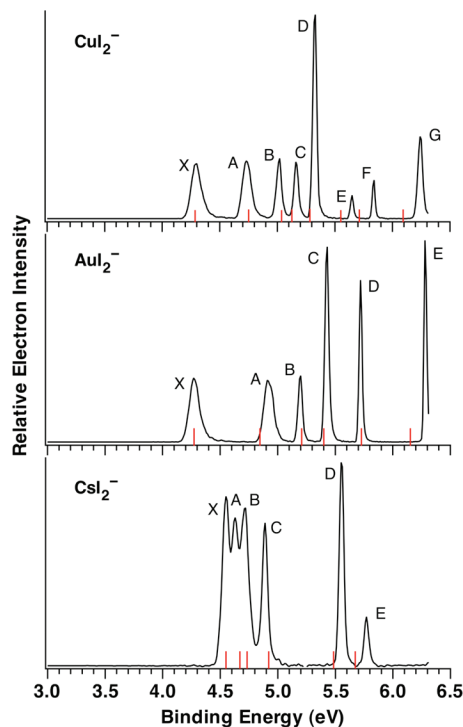


Figure 2. Photoelectron spectra of MI_2^- ($M = \text{Cs, Cu, Au}$) at 12 K and 193 nm. The short bars represent the positions of the calculated vertical detachment transitions.

CuI_2^- and AuI_2^- (Table 1), respectively, from the clearly observed 0–0 transitions. The ADE for CsI_2^- was estimated from the onset of the 12 K spectrum to be 4.52 ± 0.02 eV (Table 1).

The 193 nm spectra for MI_2^- ($M = \text{Cu, Au, Cs}$) at 12 K are shown in Figure 2. Eight well-resolved peaks, labeled X and A–G, were observed for CuI_2^- , whereas six peaks (X and A–E) spanning roughly the same energy range were resolved for AuI_2^- . Six peaks (X and A–E) were observed for CsI_2^- , with the first three peaks (X, A, B) very closely spaced. The vertical detachment energies (VDEs) for all observed peaks are given in Table 2 and compared with theoretical calculations. The MI_2^- complexes are superhalogens,³⁹ all with extremely high ADEs. The current 193 nm spectrum for AuI_2^- at 12 K is better resolved than the previous spectrum taken at room temperature.¹⁷ The current ADE of 4.226 ± 0.010 eV for AuI_2^- measured at 266 nm and 12 K is much improved relative to the value of 4.18 ± 0.07 eV measured previously at 193 nm and room temperature.¹⁷ The spectra of CuI_2^- and CsI_2^- have not been reported previously. However, they show some similarity to the PES spectra of CuBr_2^- and NaI_2^- , respectively.^{40,41}

V. Theoretical Results

We have optimized the structures and found that the MI_2^- ($M = \text{Cs, Cu, Ag, Au}$) anions are all linear with a $^1\Sigma_g^+$ ground state and $D_{\infty h}$ symmetry, consistent with previous calculations. These structures are confirmed to be minima, and the results of the vibrational analysis at the PBE level are given in Table 3. Also given in Table 3 are the optimized PBE, CCSD(T), and B3LYP bond distances and normalized vibrational frequencies (NVF) to evaluate the I–M–I bonding strengths. The Au–I distance at the CCSD(T) level is in excellent agreement with a previous calculation at a similar level of theory.¹⁹ We have also computed the vibrational frequencies for the neutral final states for AuI_2 and CuI_2 , and the calculated symmetric stretching

TABLE 2: Observed and Calculated Vertical Detachment Energies (VDEs) for MI₂⁻ (M = Cs, Cu, Ag, Au) and Final-State Assignments for M = Cs, Cu, Au

feature	final state	VDE (eV)		
		expt ^a	calcd	
CsI ₂ ⁻	X	73% [² Σ _{1/2u}], 27% [² Π _{1/2u}]	4.55	4.55 (4.63) ^b
	A	100% [² Π _{3/2u}]	4.63	4.68
	B	100% [² Π _{3/2g}]	4.72	4.72
	C	52% [² Π _{1/2g}], 48% [² Σ _{1/2g}]	4.89	4.92
	D	73% [² Π _{1/2u}], 27% [² Σ _{1/2u}]	5.55	5.49
CuI ₂ ⁻	E	52% [² Σ _{1/2g}], 48% [² Π _{1/2g}]	5.77	5.68
	X	100% [² Π _{3/2g}]	4.29	4.29 (4.47) ^b
	A	98% [² Π _{1/2g}], 2% [² Σ _{1/2g}]	4.73	4.76
	B	99% [² Σ _{1/2g}], 1% [² Π _{1/2g}]	5.02	5.03
	C	100% [² Π _{3/2u}]	5.16	5.12
AgI ₂ ⁻	D	52% [² Π _{1/2u}], 48% [² Σ _{1/2u}]	5.33	5.29
	E	100% [² Δ _{5/2g}]	5.65	5.55
	F	98% [² Δ _{3/2g}], 2% [² Π _{3/2g}]	5.84	5.71
	G	52% [² Σ _{1/2u}], 48% [² Π _{1/2u}]	6.24	6.09
		98% [² Π _{3/2g}], 2% [² Δ _{3/2g}]		6.28
		97% [² Π _{1/2g}], 3% [² Σ _{1/2g}]		6.40
		96% [² Σ _{1/2g}], 4% [² Π _{1/2g}]		7.44
		100% [² Π _{3/2g}]		4.78
		91% [² Π _{1/2g}], 9% [² Σ _{1/2g}]		5.23
		100% [² Π _{3/2u}]		5.27
AuI ₂ ⁻		52% [² Σ _{1/2u}], 48% [² Π _{1/2u}]		5.40
		91% [² Σ _{1/2g}], 9% [² Π _{1/2g}]		5.86
		52% [² Π _{1/2u}], 48% [² Σ _{1/2u}]		6.21
		100% [² Δ _{5/2g}]		7.76
		57% [² Δ _{3/2g}], 43% [² Π _{3/2g}]		8.01
		57% [² Π _{3/2g}], 43% [² Δ _{3/2g}]		8.37
		97% [² Π _{1/2g}], 3% [² Σ _{1/2g}]		8.48
		97% [² Σ _{1/2g}], 3% [² Π _{1/2g}]		8.87
	X	99% [² Π _{3/2g}], 1% [² Δ _{3/2g}]	4.28	4.28 (4.51) ^b
	A	94% [² Π _{1/2g}], 6% [² Σ _{1/2g}]	4.91	4.84
B	100% [² Π _{3/2u}]	5.20	5.21	
C	52% [² Σ _{1/2u}], 48% [² Π _{1/2u}]	5.43	5.40	
D	91% [² Σ _{1/2g}], 9% [² Π _{1/2g}]	5.72	5.73	
E	52% [² Π _{1/2u}], 48% [² Σ _{1/2u}]	6.28	6.15	
	100% [² Δ _{5/2g}]		6.16	
	52% [² Π _{3/2g}], 48% [² Δ _{3/2g}]		6.93	
	51% [² Δ _{3/2g}], 49% [² Π _{3/2g}]		7.89	
	87% [² Π _{1/2g}], 13% [² Σ _{1/2g}]		8.01	
	90% [² Σ _{1/2g}], 10% [² Π _{1/2g}]		8.82	

^a The uncertainty for the measured VDEs is ±0.02 eV. ^b The first vertical electron detachment energies (VDE₁) of MI₂⁻ (M = Cs, Cu, Au) were aligned with the experimental data for easier comparison for the higher VDEs. The theoretical VDE₁ given in parentheses were computed without including SO effects for the neutral and anionic ground states. The SO effects were included in the calculations of excitation energies for the neutral species. The higher VDEs were obtained by adding the experimental first VDE to the neutral excitation energies calculated at the geometry of the anions.

frequencies are in good agreement with the experimental observations for CuI₂ and AuI₂. The calculated VDEs are given in Table 2 for MI₂⁻ (M = Cs, Cu, Ag, Au). The first VDE in each case was calculated as the total energy difference between the neutral and anionic ground states at the anion geometry. VDEs for the excited states were computed by adding the first VDE to the excitation energies of the neutral species at the anion geometry. The calculated first VDE, given in parentheses in Table 2, was overestimated by ~0.1–0.2 eV relative to the experimental values. To facilitate comparison with the experiment in the cases of MI₂⁻ (M = Cs, Cu, Au), the first VDE was aligned with the experimental value and the higher VDEs were shifted by the differences between the calculated and experimental first VDE, as given in Table 2 and plotted in Figure 2 (vertical bars).

TABLE 3: Calculated PBE, CCSD(T), and B3LYP Bond Lengths and PBE Vibrational Frequencies for MI₂⁻ (M = Cs, Cu, Ag, Au)

	R(M–I) (Å)			vibrational frequency (cm ⁻¹)			NVF (cm ⁻¹) ^a		
	CCSD(T)		B3LYP	σ _u	σ _g	π _u	σ _u	σ _g	π _u
			PBE						
CsI ₂ ⁻	3.563	3.620	3.585	96	63	13	85	63	11
CuI ₂ ⁻	2.430	2.458	2.482	255	125 (138) ^b	62	172	125	42
AgI ₂ ⁻	2.622	2.660	2.679	196	113	48	162	113	39
AuI ₂ ⁻	2.575	2.619	2.611	196	141 (159) ^b	52	196	141	52

^a The normalized vibrational frequencies (NVF) were computed by assuming that all the metal atoms have the same mass as Au. ^b The frequencies for the neutrals are listed in parentheses. The geometry optimizations and frequency analysis are carried out with spin–orbit coupling.

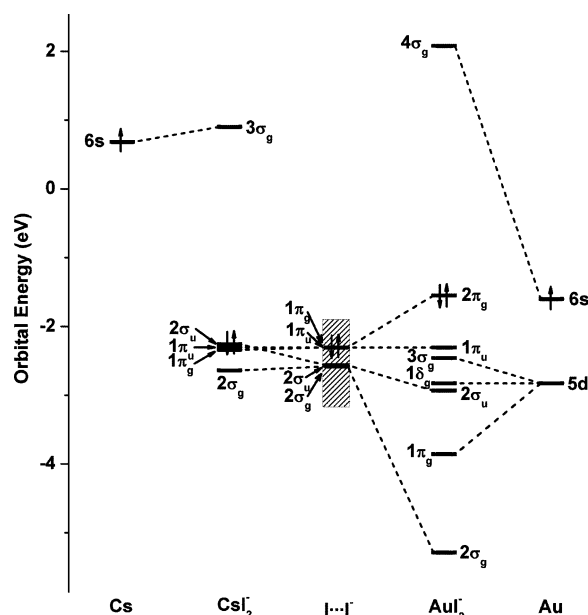


Figure 3. Orbital interactions from fragment MO analysis for MI₂⁻ (M = Cs, Au). The highest singly or doubly occupied orbitals are labeled with arrows. The orbitals of the I...I⁻ fragment have one-electron vacancy (illustrated with a diagonal grain pattern). The I–I distance in the I...I⁻ fragment is taken as the same as in the CsI₂⁻ anion. The energy levels are shifted to align all the nonbonding orbitals for the convenience of examining orbital interactions without the electrostatic effects. The 5s and 5p orbitals of Cs and Au are not counted.

We present the energy levels of the Kohn–Sham orbitals in Figure 3, which provides a qualitative understanding of the orbital interactions between M and I₂⁻ and demonstrates the ionic bonding in CsI₂⁻ versus the covalent bonding in AuI₂⁻. The isocontour surfaces of the Kohn–Sham molecular orbitals of MI₂⁻ (M = Cs, Cu, Ag, Au) are shown in Figure 4. The splittings due to SO coupling are shown in Figure 5; the σ_g and π_g (or σ_u and π_u) MOs can mix via SO interactions. The atomic charges and M–I bond orders have been analyzed using several different theoretical formalisms, as presented in Table 4. Figure 6 displays the electron localization functions (ELF) of MI₂⁻ (M = Cs, Cu, Ag, Au).⁴²

VI. Comparison between Experiment and Theory

The electronic structures of MI₂⁻ can be understood from orbital interactions or charge transfer between M and I₂⁻. Similar to the familiar valent MO patterns of the diatomic molecules, such as F₂ or I₂, the 2σ_g, 2σ_u, 1π_g, 1π_u valent manifold formed

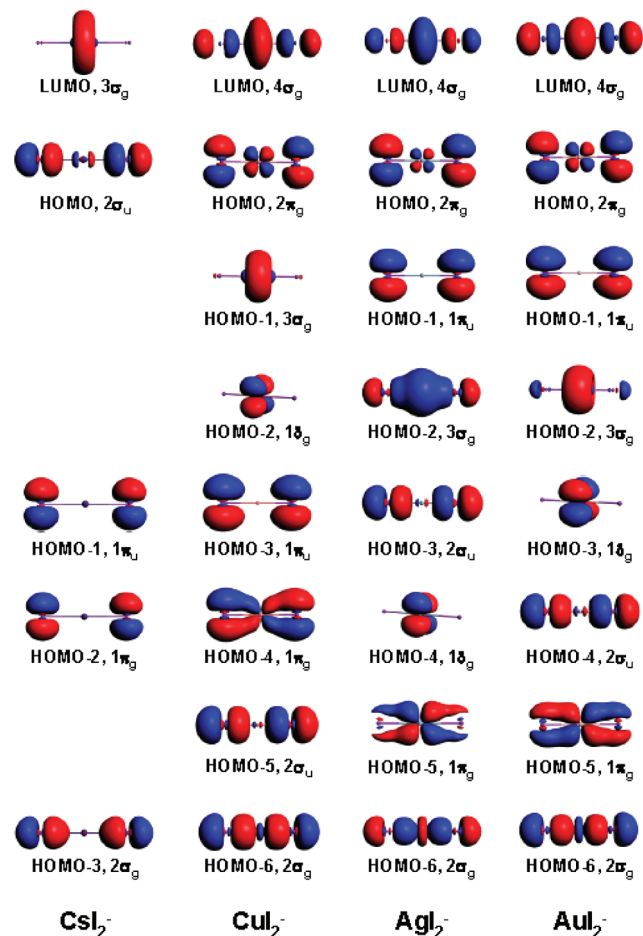


Figure 4. The isocontour surfaces of the Kahn-Sham orbitals for the MI_2^- complexes (isocontour = 0.03 au). The 5s and 5p orbitals of Cs and Au are not counted.

from the I 5p orbitals are still present in the MI_2^- systems and are split according to the nature of the $I \cdots (M) \cdots I$ interactions. As shown in Figure 3, when Cs is inserted between the two iodine atoms, the ionic interactions between Cs and I_2^- primarily lead to charge transfer from the Cs 6s orbital to the ligands and the I 5p manifold is only split by 0.9 eV. However, when Au is inserted between the two I atoms, the Au 6s and 5d_{z²} orbitals interact with the σ_g ligand orbital, giving rise to significant stabilization of $2\sigma_g$ and destabilization of $4\sigma_g$ (Figure 3). Similarly, the Au 5d π orbitals interact with the π_g ligand orbitals, leading to the stabilization of $1\pi_g$ and destabilization of $2\pi_g$. The significant orbital interactions between the Au s-d hybrids and the I 5p manifold are clear from the MO isocontour surfaces shown in Figure 4. Consequently, the I 5p manifold is split by about 4 eV in energy (Figure 3).

Figure 5 shows that there are significant SO effects for the I 5p and Au 5d orbitals, where the splittings of the spinors qualitatively reveal the respective contributions of the I 5p and Au 5d orbitals (Figure 4). The energy levels of the spinors for CsI_2^- are in qualitative agreement with the PES spectral pattern. The assignments of the PES spectra based on the SO-split states are given in Table 2; the calculated VDEs are also compared with the experimental spectra as short vertical bars in Figure 2. Overall, the calculated VDE patterns are in excellent agreement with the experimental data for all three complexes, MI_2^- ($M = Cs, Cu, Au$). The slightly inferior agreement for the high-lying excited states is a result of the limited active space employed during the expensive CASSCF calculations. The current assignments and calculated VDEs for AuI_2^- are consistent with

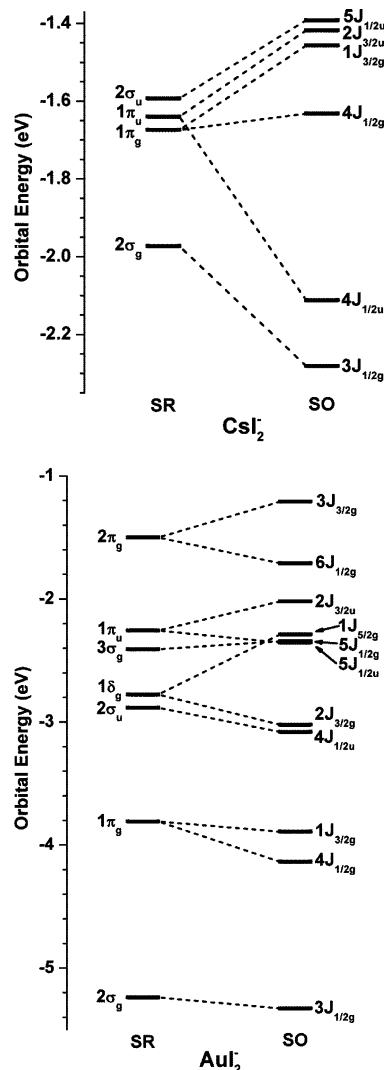


Figure 5. The SO splittings of the SR-ZORA MOs of CsI_2^- and AuI_2^- . The 5s and 5p orbitals of Cs and Au are not counted, consistent with Figures 3 and 4.

TABLE 4: Theoretical Atomic Net Charges on M and M-I Bond Orders in MI_2^- ($M = Cs, Cu, Ag, Au$)

	Charge Population				
	NPA	Hirshfeld	Voronoi	MDC-q	AIM
Cs	0.95	0.40	0.43	0.65	0.83
Cu	0.46	-0.01	-0.03	-0.08	0.31
Ag	0.48	0.03	0.05	-0.03	0.23
Au	0.24	-0.10	-0.10	-0.18	-0.08
	Bond Order				
	Wiberg	Mayer	G-J	N-M(3)	
Cs-I	0.05	0.33	0.19	1.05	
Cu-I	0.43	0.88	0.50	1.00	
Ag-I	0.41	0.77	0.49	0.99	
Au-I	0.51	0.79	0.55	0.99	

those by Misha et al. reported previously with the inclusion of SO coupling.¹⁹ We see that the HOMO of CsI_2^- is the σ_u orbital of the I_2 ligands, whereas in the three coinage diiodides the HOMO is the π_g orbital of the I_2 ligands with significant antibonding interaction with the metal d orbital. The different HOMOs for CsI_2^- and the coinage diiodides are consistent with the different angular distributions for the ground-state transitions observed in the photoelectron images (Figure 1). Further

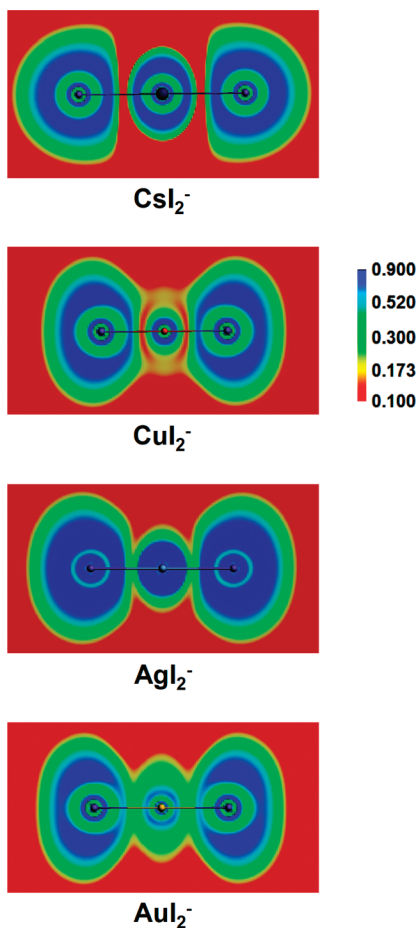


Figure 6. The electron localization functions (ELFs) for MI_2^- ($M = \text{Cs, Cu, Ag, Au}$) calculated with the PBE functional.

examination shows that the orbital orderings of CuI_2^- and AuI_2^- are also different. In particular, the $4d \sigma_g$ and δ_g MOs in CuI_2^- are higher lying, whereas they are relatively lower lying in AuI_2^- . Therefore, detachment from the δ_g MO in CuI_2^- was observed at 193 nm, corresponding to the bands E and F in Figure 2. But the δ_g MO of AuI_2^- possesses higher electron binding energies and was not accessible using the 193 nm detachment laser. As pointed out previously,^{19,43,44} SO coupling is very important to be included for Au- and I-containing compounds in order to achieve good agreement with experimental data.

VI. Discussion

The group IA elements possess a $ns^1(n-1)d^0$ configuration compared to $(n-1)d^{10}ns^1$ for the group IB elements. The filled $(n-1)d^{10}$ shell gives rise to distinct chemistry and electronic structures for group IB compounds through $s-d$ hybridization, relative to the predominantly ionic bonding in group IA compounds. Particularly, the strong relativistic effects in gold enhance the $s-d$ hybridization,¹ resulting in significant σ -covalent bonding between Au and I in AuI_2^- .

The $M-I$ bond lengths in CsI_2^- are much longer than those in AuI_2^- by about 1 Å (Table 3). In the group IB complexes, the $M-I$ bond lengths increase from Cu to Ag and then decrease from Ag to Au due to the relativistic effects in Au. The PBE $M-I$ bond lengths increase by 0.20 Å from Cu to Ag but decrease by 0.07 Å from Ag to Au. The fact that the $M-I$ bond lengths of the group IB complexes are smaller than that of Cs by about 1 Å is consistent with the atomic radii. All the $M-I$

bond lengths in the coinage diiodide complexes are within the range of the $M-I$ covalent single-bond lengths (2.45, 2.61, and 2.57 Å for Cu, Ag, Au, respectively) estimated by the self-consistent covalent radii derived by Pyykkö.⁴⁵ The optimized $\text{Au}-\text{I}$ distance of 2.58 Å at CCSD(T) level is consistent with the experimental distances in $[\text{AuI}_2]^-$ units found in crystals (2.529, 2.5604, and 2.7713 Å).⁴⁶⁻⁴⁸ The PBE-optimized $\text{Cs}-\text{I}$ distance is 0.06 Å shorter than the sum of the covalent radii.

The $M-I$ bond strengths can be measured by the vibrational frequencies of the totally symmetric stretching modes because it is not influenced by the mass of the central metal atom. Indeed, the σ_g vibrational frequency of AuI_2^- is larger than that of CsI_2^- , indicating that the $\text{Au}-\text{I}$ bonds are much stronger than the $\text{Cs}-\text{I}$ bonds. Considering the larger mass of Au than that of Ag, Cu, and Cs, we also calculated the normalized vibrational frequencies (NVF) by assuming that all the metal atoms have the same mass as Au. Both the σ_g vibrational frequencies and NVFs indicate that the $M-I$ bond strength increases as $\text{Cs}-\text{I} \ll \text{Ag}-\text{I} < \text{Cu}-\text{I} < \text{Au}-\text{I}$, which agrees well with the calculated Wiberg bond orders listed in Table 3. Note the above analyses nicely confirm the experimental observation, which shows that the symmetric stretching frequency of AuI_2^- is slightly higher than that of CuI_2^- .

The charge population and bond order analyses for MI_2^- ($M = \text{Cs, Cu, Ag, Au}$) given in Table 4 reveal that all the methods predict much less positive charge on the group IB-metal atoms than on Cs, indicating that Cu, Ag, and Au have covalent character in contrast to the ionic bonding in CsI_2^- . The AuI_2^- complex is especially interesting: All the charge population formalisms except natural population analysis (NPA) predict negative charges on the Au atom. This slightly negative charge on Au is consistent with the strong $s-d$ hybridization of Au and the much stronger covalent bonding in the AuI_2^- complex than in its lighter congeners. Except the $N-M(3)$ bond order, which includes ionic interactions, all the calculated bond orders are larger for $M-I$ ($M = \text{Cu, Ag, Au}$) than for the $\text{Cs}-\text{I}$ bond, indicating that the $\text{Cs}-\text{I}$ bond is ionic whereas the coinage complexes have more covalent character, with $\text{Au}-\text{I}$ having the strongest covalent bonding.

The electron localization functions (ELFs) shown in Figure 6 reflect the electron pair density in the MI_2^- complexes, which provide further insight into the nature of the bonding between M and I. In covalent bonding the forces binding the nuclei are exerted by an increase in the charge density shared mutually between the two atoms, whereas in ionic bonding the two atoms are bound by increased cationic or anionic charges localized in the region of each nucleus. As shown in Figure 6, there is no electron pair density between the Cs and I atoms, as expected from their ionic bonding. Significant electron pair density exists between the $M-I$ ($M = \text{Cu, Ag, Au}$) bonds, increasing from Cu to Au and suggesting relatively strong covalent character.

The different bonding nature between the groups IA and IB compounds can also be glimpsed from the orbital interaction analysis (Figure 3). In CsI_2^- , the Cs $6s^1$ orbital is much higher in energy than the frontier 5p orbitals of $\text{I}\cdots\text{I}^-$, resulting in an electron transfer from Cs to $\text{I}\cdots\text{I}^-$ and the formation of an ionic compound $[(\text{I}^-)\text{Cs}^+(\text{I}^-)]$. Their orbital interactions are weak, and the energy levels of the I 5p manifold change very little from the fragments to the CsI_2^- complex. The AuI_2^- complex is quite different. Because the energy of the Au $6s^1$ orbital is much closer to that of the frontier 5p orbitals of $\text{I}\cdots\text{I}^-$, the strong orbital interactions lower the occupied $2\sigma_g$ orbital and lift the unoccupied $4\sigma_g$ orbital significantly. The directional $5d_{z^2}$ orbitals of Au can hybridize with the 6s orbital, promoting orbital

overlap to form the Au–I covalent bonds. The 3d orbitals of Cu are more tightly contracted in the radial distribution while the energy gap between Ag 4d and 5s is considerably large, thus the s–d hybridization is relatively unfavorable for Cu and Ag than for Au, as confirmed by the charge population, bond order, and ELF analyses. Therefore, the series of MI_2^- ($M = Cs, Cu, Ag, Au$) complexes investigated here provide a gradual transition from ionic bonding in CsI_2^- to covalent bonding in AuI_2^- .

It is also interesting to compare the covalent bonding in AuI_2^- with that of AuO_2^- or AuS_2^- , which were reported recently to possess linear structures with multiple covalent bonding character.⁸ The valent MOs of AuI_2^- are similar to those in AuO_2^- or AuS_2^- . However, the latter is two electrons fewer and the $2\pi_g$ MO is half-filled. As seen in Figure 4, the $2\pi_g$ MO is antibonding, which cancels out the bonding interaction of the $1\pi_g$ MO. Because the $2\pi_g$ MO is half-filled in AuO_2^- or AuS_2^- , there is net π bonding in these two molecules, giving rise to multiple bonding character. However, both the $2\pi_g$ and $1\pi_g$ MOs are fully occupied in AuI_2^- and they cancel each other, leaving only a single σ bond between Au and I. Just like in $Au(CN)_2^-$, the covalent bonding imparts significant stability to AuI_2^- . This conclusion is consistent with the fact that AuI_2^- is a highly stable complex in solution and, unlike $AuBr_2^-$ or $AuCl_2^-$, it does not undergo disproportionate reactions.⁴⁹

VII. Conclusions

A series of metal diiodide complex, MI_2^- ($M = Cs, Cu, Ag, Au$), have been studied both experimentally and theoretically to examine the metal–iodine chemical bonding. Photoelectron imaging and low-temperature photoelectron spectroscopy were used to obtain vibrational and electronic structure information, yielding accurate electron affinities, 4.52 ± 0.02 , 4.256 ± 0.010 , and 4.226 ± 0.010 eV for CsI_2 , CuI_2 , and AuI_2 , respectively, and well-resolved detachment transitions to the ground and excited states of the neutral MI_2 complexes. Spin–orbit coupling is found to be important in these systems. Theoretical vertical detachment energies computed using the CASSCF/CCSD(T)/SO approach allow quantitative assignments of all spectral transitions. Chemical bonding analyses, including charge populations, bond orders, electron localization functions, and orbital interactions reveal a transition from typical ionic bonding character in CsI_2^- to relatively strong covalent bonding in AuI_2^- .

Acknowledgment. The experimental work was supported by the National Science Foundation (CHE-1036387) and by the U.S. Department of Energy (DOE), Office of Basic Energy Sciences, Division of Chemical Sciences, Geosciences and Biosciences, and partly performed at the W. R. Wiley Environmental Molecular Sciences Laboratory, a national scientific user facility sponsored by DOE's Office of Biological and Environmental Research and located at Pacific Northwest National Laboratory, which is operated for the DOE by Battelle. The theoretical work was supported by NKBRFSF (2006CB932305, 2007CB815200) and NSFC (20933003) in China. The calculations were performed using the DeepComp 7000 Supercomputer at the Computer Network Information Center, Chinese Academy of Sciences and the Shanghai Supercomputing Center.

References and Notes

- (1) Pyykkö, P. *Chem. Rev.* **1988**, *88*, 563.
- (2) Schwarz, H. *Angew. Chem., Int. Ed.* **2003**, *42*, 4442.
- (3) Pyykkö, P. *Angew. Chem., Int. Ed.* **2004**, *43*, 4412.
- (4) Wang, L. S. *Phys. Chem. Chem. Phys.* **2010**, DOI: 10.1039/C003886E.
- (5) Dietz, O.; Rayón, V. M.; Frenking, G. *Inorg. Chem.* **2003**, *42*, 4977.
- (6) Zaleski-Eigierd, P.; Patzschke, M.; Pyykkö, P. *J. Chem. Phys.* **2008**, *128*, 224303.
- (7) Wang, X. B.; Wang, Y. L.; Yang, J.; Xing, X. P.; Li, J.; Wang, L. S. *J. Am. Chem. Soc.* **2009**, *131*, 16368.
- (8) Zhai, H. J.; Bürgel, C.; Bonacic-Koutecky, V.; Wang, L. S. *J. Am. Chem. Soc.* **2008**, *130*, 9156.
- (9) Söhnel, T.; Hermann, H.; Schwerdtfeger, P. *J. Phys. Chem. B* **2005**, *109*, 526.
- (10) Schulz, A.; Hargittai, M. *Chem.—Eur. J.* **2001**, *7*, 3657.
- (11) Söhnel, T.; Brown, R.; Kloo, L.; Schwerdtfeger, P. *Chem.—Eur. J.* **2001**, *7*, 3167.
- (12) Schwerdtfeger, P.; Krawczyk, R. P.; Hammerl, A.; Brown, R. *Inorg. Chem.* **2004**, *43*, 6707.
- (13) Schwerdtfeger, P.; McFeaters, J. S.; Liddell, M. J.; Hrušák, J.; Schwarz, H. *J. Chem. Phys.* **1995**, *103*, 245.
- (14) Seth, M.; Cooke, F.; Schwerdtfeger, P.; Heully, J. L.; Pelissier, M. *J. Chem. Phys.* **1998**, *109*, 3935.
- (15) Brown, J. R.; Schwerdtfeger, P.; Schroder, D.; Schwarz, H. *J. Am. Soc. Mass Spectrom.* **2002**, *13*, 485.
- (16) Mishra, S. *Phys. Chem. Chem. Phys.* **2008**, *10*, 3987.
- (17) Schröder, D.; Brown, R.; Schwerdtfeger, P.; Wang, X. B.; Yang, X.; Wang, L. S.; Schwarz, H. *Angew. Chem., Int. Ed.* **2003**, *42*, 311.
- (18) Dai, B.; Yang, J. *Chem. Phys. Lett.* **2003**, *379*, 512.
- (19) Mishra, S.; Vallet, V.; Domcke, W. *ChemPhysChem* **2006**, *7*, 723.
- (20) Mishra, S. *J. Phys. Chem. A* **2007**, *111*, 9164.
- (21) Xing, X. P.; Wang, X. B.; Wang, L. S. *J. Chem. Phys.* **2009**, *130*, 074301.
- (22) Wang, X. B.; Wang, L. S. *Rev. Sci. Instrum.* **2008**, *79*, 073108.
- (23) Wang, L. S.; Ding, C. F.; Wang, X. B.; Barlow, S. E. *Rev. Sci. Instrum.* **1999**, *70*, 1957.
- (24) Dribinski, V.; Ossadchi, A.; Mandelshtam, V. A.; Reisler, H. *Rev. Sci. Instrum.* **2002**, *73*, 2634.
- (25) Perdew, J. P.; Burke, K.; Ernzerhof, M. *Phys. Rev. Lett.* **1996**, *77*, 3865.
- (26) ADF 2009.01, SCM, Theoretical Chemistry, Vrije Universiteit, Amsterdam, The Netherlands (<http://www.scm.com>). (a) te Velde, G.; Bickelhaupt, F. M.; Baerends, E. J.; Guerra, C. F.; van Gisbergen, S. J. A.; Snijders, J. G.; Ziegler, T. *J. Comput. Chem.* **2001**, *22*, 931. (b) Guerra, C. F.; Snijders, J. G.; te Velde, G.; Baerends, E. J. *Theor. Chem. Acc.* **1998**, *99*, 391.
- (27) van Lenthe, E.; Baerends, E. J. *J. Comput. Chem.* **2003**, *24*, 1142.
- (28) van Lenthe, E.; Baerends, E. J.; Snijders, J. G. *J. Chem. Phys.* **1993**, *99*, 4597.
- (29) Frisch, M. J.; Trucks, G. W.; Schlegel, H. B.; Scuseria, G. E.; Robb, M. A.; Cheeseman, J. R.; Montgomery, J. A., Jr.; Vreven, T.; Kudin, K. N.; Burant, J. C.; Millam, J. M.; Iyengar, S. S.; Tomasi, J.; Barone, V.; Mennucci, B.; Cossi, M.; Scalmani, G.; Rega, N.; Petersson, G. A.; Nakatsuji, H.; Hada, M.; Ehara, M.; Toyota, K.; Fukuda, R.; Hasegawa, J.; Ishida, M.; Nakajima, T.; Honda, Y.; Kitao, O.; Nakai, H.; Klene, M.; Li, X.; Knox, J. E.; Hratchian, H. P.; Cross, J. B.; Adamo, C.; Jaramillo, J.; Gomperts, R.; Stratmann, R. E.; Yazyev, O.; Austin, A. J.; Cammi, R.; Pomelli, C.; Ochterski, J. W.; Ayala, P. Y.; Morokuma, K.; Voth, G. A.; Salvador, P.; Dannenberg, J. J.; Zakrzewski, V. G.; Dapprich, S.; Daniels, A. D.; Strain, M. C.; Farkas, O.; Malick, D. K.; Rabuck, A. D.; Raghavachari, K.; Foresman, J. B.; Ortiz, J. V.; Cui, Q.; Baboul, A. G.; Clifford, S.; Cioslowski, J.; Stefanov, B. B.; Liu, G.; Liashenko, A.; Piskorz, P.; Komaromi, I.; Martin, R. L.; Fox, D. J.; Keith, T.; Al-Laham, M. A.; Peng, C. Y.; Nanayakkara, A.; Challacombe, M.; Gill, P. M. W.; Johnson, B.; Chen, W.; Wong, M. W.; Gonzalez, C.; Pople, J. A. *Gaussian 03, Revision A.1*; Gaussian, Inc.: Wallingford, CT, 2003.
- (30) Werner, H.-J. *MOLPRO, Version 2008.1*, a package of ab initio programs; see: <http://www.molpro.net>.
- (31) (a) Purvis, G. D.; Bartlett, R. J. *J. Chem. Phys.* **1982**, *76*, 1910. (b) Scuseria, G. E.; Janssen, C. L.; Schaefer, H. F. *J. Chem. Phys.* **1988**, *89*, 7382.
- (32) (a) Roos, B. O.; Taylor, P. R.; Siegbahn, P. E. M. *Chem. Phys.* **1980**, *48*, 157. (b) Roos, B. O. *Int. J. Quantum Chem.* **1980**, *S14*, 175.
- (33) Berning, A.; Schweizer, M.; Werner, H.-J.; Knowles, P. J.; Palmieri, P. *Mol. Phys.* **2000**, *98*, 1823.
- (34) Lim, I. S.; Schwerdtfeger, P.; Metz, B.; Stoll, H. *J. Chem. Phys.* **2005**, *122*, 104103.
- (35) Peterson, K. A.; Puzzarini, C. *Theor. Chem. Acc.* **2005**, *114*, 283.
- (36) Peterson, K. A.; Shepler, B. C.; Figgen, D.; Stoll, H. *J. Phys. Chem. A* **2006**, *110*, 13877.
- (37) Figgen, D.; Rauhut, G.; Dolg, M.; Stoll, H. *Chem. Phys.* **2005**, *311*, 227.
- (38) Hay, P. J. *J. Chem. Phys.* **1977**, *66*, 4377.
- (39) (a) Gutsev, G. L.; Boldyrev, A. I. *Chem. Phys.* **1981**, *56*, 277. (b) Gutsev, G. L.; Boldyrev, A. I. *Adv. Chem. Phys.* **1985**, *61*, 169.
- (40) Wang, X. B.; Wang, L. S.; Brown, R.; Schwerdtfeger, P.; Schröder, D.; Schwarz, H. *J. Chem. Phys.* **2001**, *114*, 7388.

- (41) Wang, X. B.; Ding, C. F.; Wang, L. S.; Boldyrev, A. I.; Simons, J. *J. Chem. Phys.* **1999**, *110*, 4763.
- (42) (a) Becke, A. D.; Edgecombe, K. E. *J. Chem. Phys.* **1990**, *92*, 5397.
(b) Savin, A.; Flad, J.; Preuss, H.; Jepsen, O.; Andersen, O. K.; von Schnering, H. G. *Angew. Chem.* **1992**, *104*, 186.
- (43) Huang, W.; Bulusu, S.; Pal, R.; Zeng, X. C.; Wang, L. S. *J. Chem. Phys.* **2009**, *131*, 234305.
- (44) Huang, W.; Pal, R.; Wang, L. M.; Zeng, X. C.; Wang, L. S. *J. Chem. Phys.* **2010**, *132*, 054305.
- (45) (a) Pyykkö, P.; Riedel, S.; Patzschke, M. *Chem.—Eur. J.* **2005**, *11*, 3511. (b) Pyykkö, P.; Atsumi, M. *Chem.—Eur. J.* **2009**, *15*, 186. (c) Pyykkö, P.; Atsumi, M. *Chem.—Eur. J.* **2009**, *15*, 12770.

- (46) Wang, H. H.; Montgomery, L. K.; Geiser, U.; Porter, L. C.; Carlson, K. D.; Ferraro, J. R.; Williams, J. W.; Cariss, C. S.; Rubinstein, R. L.; Whitworth, J. R.; Evain, M.; Novoa, J. J.; Whangbo, M.-H. *Chem. Mater.* **1989**, *1*, 140.
- (47) Kaska, W. C.; Mayer, H. A.; Elsegood, M. R. J.; Horton, P. N.; Hursthouse, M. B.; Redshaw, C.; Humphrey, S. M. *Acta Crystallogr., Sect. E* **2004**, *60*, m563.
- (48) Angle, C. S.; Woolard, K. J.; Kahn, M. I.; Golen, J. A.; Rheingold, A. L.; Doerrer, L. H. *Acta Crystallogr., Sect. C* **2007**, *63*, m231.
- (49) Cotton, F. A.; Wilkinson, G. *Advanced Inorganic Chemistry*, 5th ed.; Wiley & Sons: New York, 1988; p 948.

JP103173D